Dalton Transactions

ROYAL SOCIETY OF CHEMISTRY

PAPER

View Article Online
View Journal | View Issue

Cite this: *Dalton Trans.*, 2025, **54**, 16562

Sodium lanthanide tungstate-based nanoparticles as bimodal probes for T_1–T_2 magnetic resonance imaging and X-ray computed tomography

Elisabet Gómez-González, *[a] Nuria O. Núñez, [a] Carlos Caro, [b,c] Maria L. García-Martín, [b,c] José M. Monje Moreno, [d] Amel Hamdi,[e] Pilar López-Larrubia,[f] Ana I. Becerro [a] and Manuel Ocaña *[a]

Magnetic resonance imaging (MRI) is one of the most commonly used imaging techniques for diagnosis in clinics. Often, magnetically-active substances, called contrast agents (CAs), have to be used, which increase contrast by shortening the longitudinal (T_1) (resulting in signal enhancement in T_1-weighted images) and/or transverse (T_2) (resulting in signal decay in T_2-weighted images) relaxation times of the water protons present in biological tissues. A further strategy to improve diagnostic accuracy is recording both kinds of images (T_1-weighted and T_2-weighted) using dual T_1–T_2 CAs, which facilitates the exclusion of false positives. The traditional T_1 or T_2 contrast agents are not suitable for such a purpose. This paper deals with the development of double sodium lanthanide tungstate-based nanoparticles containing Gd^{3+} and Dy^{3+} cations, which are dispersible in physiological media, do not show appreciable *in vitro* (for human fibroblast cells) and *in vivo* (for *C. elegans*) toxicity and present appropriate relaxivity values for their use as a dual T_1–T_2 contrast agent for magnetic resonance imaging. In addition, they show an excellent X-ray attenuation capacity, thanks mainly to their tungsten content, which makes them also useful for X-ray computed tomography. Hence, the developed nanoparticles are ideal multimodal probes to be used as a dual T_1–T_2 contrast agent for magnetic resonance imaging and as a contrast agent for X-ray computed tomography.

Received 12th August 2025,
Accepted 6th October 2025

DOI: 10.1039/d5dt01925g

rsc.li/dalton

Introduction

Nowadays, magnetic resonance imaging (MRI) is one of the most commonly used imaging techniques for diagnosis in clinics, whose main advantages are its non-invasive character, excellent spatial resolution and high imaging depth.[1] Often, the contrast difference between the region of interest (ROI) and its surroundings is not enough to get relevant information. In these cases, the so-called contrast agents (CAs) are used, which increase contrast by shortening the longitudinal (T_1) and/or transverse (T_2) relaxation times of the water protons present in biological tissues. In the first case, the ROI appears brighter, for which the CAs are called positive, whereas in the second case, the ROI becomes darker, and the CAs are called negative. The efficacy of a CA is given by its longitudinal (r_1) and transverse (r_2) magnetic relaxivity values, which are defined as the increase in longitudinal or transverse relaxation rates per unit concentration of the CA. The ideal positive CAs should present an r_2/r_1 ratio close to 1,[2–4] while for ideal negative CAs, this ratio should be >10.[2,3] Currently, the most relevant positive CAs are based on Gd^{3+} complexes, which are the most commonly used in clinical settings, whereas the most studied T_2 CAs are based on superparamagnetic iron oxide-based NPs (SPIONs).[5]

Although the MRI technique using T_1 or T_2 CAs is well established in clinical practice, several innovations are currently being proposed to further improve diagnostic accuracy. Among them, recording T_1-weighted and T_2-weighted images using dual T_1–T_2 CAs has been reported to be a suitable strategy to exclude false positives by cross-validation of both types of images.[6] It has been reported that for such a purpose, the MRI CAs should present r_2/r_1 values between those that are ideal for T_1 and T_2 CAs (in the 1–10 range).[4] Unfortunately, the traditional CAs mentioned above do not fulfill such a require-

[a]*Instituto de Ciencia de Materiales de Sevilla (CSIC-US), c/Américo Vespucio, 49, 41092 Sevilla, Spain. E-mail: mjurado@icmse.csic.es, elisabet.gomez@icmse.csic.es*
[b]*Biomedical Magnetic Resonance Laboratory-BMRL, Andalusian Public Foundation Progress and Health-FPS, Seville, Spain*
[c]*Instituto de Investigación Biomédica de Málaga y Plataforma en Nanomedicina - IBIMA Plataforma BIONAND, and CIBER-BBN, Málaga 29590, Spain*
[d]*Centro Andaluz de Biología del Desarrollo (CABD), Universidad Pablo de Olavide (UPO), Molecular Biology and Biochemical Engineering Department, CSIC/UPO/JA, Carretera de Utrera Km1, 41013-Sevilla, Spain*
[e]*Phytochemicals and Food Quality Group, Instituto de la Grasa, Consejo Superior de Investigaciones Científicas (CSIC), Pablo de Olavide Universitary Campus, Building 46, Carretera de Utrera Km 1, 41013-Seville, Spain*
[f]*Instituto de Investigaciones Biomédicas Sols-Morreale (IIBM), CSIC-UAM, Madrid, Spain*

ment, so it is essential to develop new CAs. Recently, it has been shown that some CAs made of manganese ferrites[7] or Mn–Co spinels[8] and ultra-small SPIONs can shorten both T_2 and T_1 and work as dual T_1–T_2 agents,[9] although the capability to shorten T_1 of the latter is much lower.[10] Another class of dual T_1–T_2 CAs proposed combines a positive and a negative CA within the same NP. Examples are those containing SPIONs (T_2 component) loaded with Gd^{3+} complexes (T_1 component) or those containing two types of lanthanide cations (Ln^{3+}), with Gd^{3+} working as a T_1 agent thanks to its high spin angular momentum (7/2) and Dy^{3+} or Ho^{3+}, which behave as T_2 agents due to their high magnetic moments (10.65 μB for Dy^{3+} and 10.0 μB for Ho^{3+}).[11–14] The latter are advantageous from the synthesis point of view since the similar reactivity of Ln^{3+} ions towards precipitation would simplify the synthesis processes. Most combinations of Gd^{3+} with either Dy^{3+} or Ho^{3+} proposed in the literature are based on fluoride matrices,[15–20] which have a certain solubility in aqueous media[21,22] and are therefore potentially toxic.[23] It is, therefore, of great interest to develop new lanthanide-containing dual CAs based on other types of compounds, among which oxide[24] and vanadate have already been reported.[25]

Another suggested strategy to obtain a more reliable medical diagnosis is to combine MRI with other complementary imaging techniques, such as X-ray computed tomography (CT), which is commonly used for hard tissue imaging, while MRI is more suitable for soft tissue imaging.[26] To obtain both kinds of images, a multimodal CA would be advantageous to minimize possible adverse effects on the patient. In this sense, the above-mentioned lanthanide-based MRI CAs would also be ideal for CT imaging since the high atomic number (Z) of lanthanides confers a high X-ray absorption attenuation capability to such compounds.[27,28] In fact, multimodal NPs based on fluoride[15] and oxide[24] matrices containing Gd^{3+} and Dy^{3+} ions suitable as dual T_1–T_2 MRI and CT CAs have already been reported. Nevertheless, it can be assumed that the incorporation of such Ln^{3+} cations into matrices containing elements with much higher Z values than fluorine (Z = 9) or oxygen (Z = 8) such as tungsten (Z = 74) would greatly improve the CT performance of such multimodal CAs. However, to the best of our knowledge, no report regarding this kind of multimodal CA based on tungsten-containing phases can be found in the literature.

It is important to mention that nanoparticulated CAs for bioimaging must present a homogeneous size and shape, be non-toxic, and be dispersible in physiological media.[29] The latter property is usually achieved by coating the NPs with different polymers, among which polyacrylic acid (PAA) has been shown to be very efficient for such a purpose for many nanoparticulated bioprobes, including T_1–T_2 CAs.[8]

This work aimed to develop a tungstate-based nanoparticulate bimodal probe surface modified with PAA, suitable as a CT CA and as a dual T_1–T_2 MRI CA using Gd^{3+} and Dy^{3+} as T_1 and T_2 components, respectively. For such a purpose, the pursued NPs containing both Ln^{3+} cations in solid solution were synthesized by a wet chemical method based on a homogeneous precipitation process in ethylene glycol (EG)/water media. To assess the suitability of such NPs for the intended bioimaging applications, their r_1 and r_2 relaxivities at different magnetic fields and the X-ray attenuation properties were first measured, and then their dispersibility in several physiological media and their biocompatibility were evaluated. The latter assays were performed both *in vitro* using the human foreskin fibroblast cell line (HFF-1) and *in vivo* using the nematode *Caenorhabditis elegans* (*C. elegans*). Although rodent models are physiologically closer to humans, making them highly relevant for biomedical translation, *C. elegans* is a very useful animal model to evaluate the interactions between biological systems and NPs[30–32] due to its advantages, which include a rapid life cycle, a short lifespan, transparency, and facile and inexpensive growth in Petri dishes.

Experimental

Reagents

Dysprosium nitrate pentahydrate ($Dy(NO_3)_3{\cdot}5H_2O$, Sigma Aldrich, 99.99%), gadolinium nitrate hexahydrate ($Gd(NO_3)_3{\cdot}6H_2O$, Sigma Aldrich, 99.9%) and sodium tungstate dihydrate ($Na_2WO_4{\cdot}2H_2O$, Sigma Aldrich, ≥99%) were used as precursors. Ethylene glycol (EG, Sigma Aldrich, 99.8%) was used as a solvent. Polyacrylic acid (PAA, Sigma Aldrich, M_w 1800) was used for NP functionalization. These chemicals were used as received.

A 2-(*N*-morpholino)ethanesulfonic acid buffer (pH 6.5) solution (50 mM) was prepared by dissolving the needed amount of MES (Sigma-Aldrich) in Milli-Q water. Saline solution (Sigma-Aldrich) was utilized in its original form. Iohexol (≥95%) was acquired from Sigma-Aldrich.

Human foreskin fibroblasts (HFF-1; ATCC SCRC-1041) were purchased from the American Type Culture Collection (ATCC).

C. elegans Bristol strain N2 and *Escherichia coli* OP50 used for *in vivo* toxicity studies were acquired from the *Caenorhabditis* Genetics Center (CGC) stock collection (University of Minnesota, St Paul, MN, USA). The nematode growth medium (NGM) and M9 buffer (M9) were prepared as previously described.[33] Glutaraldehyde (Grade I, 25% in H_2O, Sigma-Aldrich), sodium cacodylate buffer (Sigma-Aldrich), osmium tetroxide (Sigma-Aldrich), and a Spurr low-viscosity hydrophobic resin (Sigma-Aldrich) were used to prepare the nematode samples for TEM observations.

Nanoparticle synthesis

The Gd^{3+}–Dy^{3+} tungstate-based NPs were synthesized through a homogeneous precipitation process in a mixed EG/H_2O media, by adapting a procedure previously reported by us for the synthesis of single $NaDy(WO_4)_2$ NPs,[34] which was modified to account for the different NP compositions. The detailed synthesis protocol was as follows. Dysprosium nitrate pentahydrate and gadolinium nitrate hexahydrate were dissolved in 8 mL of EG under magnetic stirring at 80 °C to achieve a solution with a concentration of 0.02 M for each of the Ln^{3+}

cations so that the Gd/Dy mol ratio was equal to 1, following a previous report on Gd–Dy mixed oxide NPs.[24] The solution was cooled to room temperature and mixed with 2 mL of a 0.1 M Na_2WO_4 aqueous solution containing 2 mg mL^{-1} of PAA. The mixture was stirred with a magnet for 1 minute at room temperature for homogenization, after which it was introduced in sealed test tubes and aged at 220 °C for 1 hour in a microwave-assisted oven (Monowave 300, Anton Paar). The obtained precipitate was cooled down to room temperature and washed by centrifugation, twice with ethanol and once with double distilled water. After purification, the NPs were either dispersed in distilled water or dried at 50 °C for further analysis.

Characterization techniques

A JEOL 2100Plus transmission electron microscope (TEM) was used to assess the morphology of particles. The images were obtained by placing a droplet of NPs suspended in water on a copper grid coated with a transparent polymer. Particle size histograms were obtained from the TEM images by counting about one hundred particles and using ImageJ open-access software.

Dynamic Light Scattering (DLS) was used to assess the dispersibility and colloidal stability of the NPs in the selected media (water, MES, and saline) by using a Malvern Zetasizer Nano-ZS90. The NP content in such dispersions was 0.5 mg mL^{-1}.

X-ray diffraction (XRD) patterns were obtained using a PANalytical X'Pert Pro diffractometer (Cu Kα) with an X'Celerator detector. The measurement conditions were: angular range (2θ) between 10° and 90°, counting time = 10 s, and 2θ step width = 0.03°.

A Jasco FT/IR-6200 Fourier transform spectrometer was employed to record the Fourier-transform infrared (FTIR) spectra of the NPs embedded in KBr pellets.

Thermogravimetric analyses (TGAs) were conducted at a heating rate of 10 °C min^{-1} in an air atmosphere using a TA Instruments SDT Q600.

Inductively coupled plasma (ICP) was used to analyze the NP composition and the NP concentration in aqueous dispersions. For that, the NPs were dissolved in concentrated hydrochloric acid (overnight at room temperature) and the obtained solutions were analyzed in a Thermo Fisher Scientific iCAP 7200 ICP-OES Duo instrument.

Magnetic relaxivities

Longitudinal, r_1, and transverse, r_2, relaxivities were estimated from the slope of the line obtained by plotting the relaxation rate ($R_i = 1/T_i$, $i = 1, 2$) *versus* total Ln^{3+} concentration, using aqueous dispersions with different NP concentrations. Relaxation times were measured at 1.44 T using a Bruker Minispec Time Domain Nuclear Magnetic Resonance (TD-NMR) instrument, and at 3 T using a MR Solutions scanner (MR Solutions Ltd, Guildford, UK) equipped with a gradient insert of 560 mT m^{-1} and a 40 mm bore radiofrequency coil. T_1 maps were generated from T_1-weighted images acquired with a saturation-recovery spin-echo sequence with 7 TR values (from 100 to 8000 ms), TE = 11 ms, and a total acquisition time of 30 min. T_2 maps were obtained by using a CPMG spin-echo sequence with TR = 5000 ms, 64 TE values (from 10 to 640 ms), and a total acquisition time of 10 min 40 s. The corresponding relaxation maps were generated employing in-house scripts developed in Python.

X-ray computed tomography (CT)

The x-ray absorption attenuation properties of NP suspensions or iohexol solutions, with different CA contents and introduced in Eppendorf tubes, were evaluated using a ZEISS Xradia 610 Versa 3D X-ray microscope (XRM) with a 0.4× objective lens, resulting in a pixel size of 213 μm (no filter was used). The acquisition conditions included a current of 123 μA, a voltage of 70 kVp, and an exposure time of 0.1 s. The software Reconstructor Scout and Scan 16.1.13.038 was used to reconstruct the images from 801 projections. Such images were analysed using ImageJ software, using a spherical volume with a radius of 0.5 cm. To calibrate images, the water X-ray attenuation intensity was set at 0 Hounsfield units (HU), while air attenuation was set at −1000 HU.

Cytotoxicity evaluation

The NP biocompatibility was evaluated by analyzing mitochondrial activity, cell morphology, and the quantity of necrotic/late apoptotic cells through MTT and live-dead tests performed using human foreskin fibroblasts (HFF-1) and following methods previously described by members of our team.[35]

Statistical analysis of the cell culture experiments was performed using Jamovi software (version 2.3.21). The Mann–Whitney U test was selected for non-parametric assessment. Data are presented as mean ± standard deviation (SD).

In vivo toxicity

For *C. elegans* exposure to NPs, young larvae at the first stage (L1) were collected 24 hours after being placed in M9 under agitated conditions at 20 °C, following a bleaching treatment of pregnant hermaphrodite adults. Approximately 300 young larvae were seeded in multiple plates. The worms were cultivated until they reached the young adult stage, typically after 52 hours at a temperature of 20 °C. The samples were then recovered using fresh Milli-Q water and washed three times. The worms were subjected to NPs diluted in Milli-Q water at various final concentrations and left to incubate for 24 hours under agitation at 20 °C.

Two toxicological tests were conducted, one measuring survival (lethal endpoint) and the other assessing brood size (sub-lethal endpoint). In the survival assay, young adults were exposed to either Milli-Q water alone (untreated worms used as a control) or varying concentrations of NPs dispersed in Milli-Q water (treated worms) in 96-well plates for 24 hours, with 48 wells per condition and 100 μL per well. The test was conducted four times. The plates were tapped, and the worms that showed movement were considered alive. In the event of uncertainty, the worms were probed using a picking needle. Each well held between 10 and 30 adult worms. Worm survival

is presented as the proportion of live worms compared to the untreated group. In the brood size test, treated adult worms, as mentioned before, were transferred to NGM plates seeded with an OP50 lawn at 20 °C to examine brood size (one per plate). Progeny was assessed 48 hours after the resumption of feeding and left overnight at 16 °C to enable egg hatching. The results are presented as the proportion of brood size compared to worms that did not receive any treatment. The reproductive toxicity assay was conducted three times with at least 20 worms per condition.

TEM analyses were also conducted to assess the nematode's capacity for consuming NPs. For that, the treated worms were rinsed three times with Milli-Q water and then preserved in 2.5% glutaraldehyde for 2 hours. Then, three washing steps were conducted using a 0.2 M sodium cacodylate buffer solution, each lasting 20 minutes, and the samples were stored at a temperature of 4 °C. Afterwards, double fixation with 1% osmium tetroxide was performed, followed by three washing steps with distilled water, a treatment with 2% uranyl, and an increasing dehydration process in up to 100% acetone. The fixed samples were placed in Spurr resin and polymerized at 70 °C for 7 h. Once the blocks were obtained, they were cut using a Leica UC7 ultramicrotome, and 70 nm cuts were made using Cu200 hexagonal grids. Previously, 350 nm cuts were made to check the correct area. Finally, the slices were observed using a Zeiss Libra 120 transmission electron microscope operated at 80 kV.

For pictures of the adult animals, we used a Zeiss Axio Imager M2 fluorescence microscope. Worms exposed to NPs were placed in a 2% agarose pad with 10 mM levamisole as an anaesthetic and placed under the microscope with a 5× objective.

Results and discussion

Synthesis and characterization of single-phase NPs

The particles obtained as described in the Experimental section showed a quasi-equiaxial shape (Fig. 1a) with a mean diameter of 30 nm and a narrow size distribution (standard deviation, $\sigma = 6$) (Fig. 1b).

The XRD pattern of these NPs (Fig. 2a) showed a set of reflections that matched well with the PDF file for tetragonal $NaGd(WO_4)_2$ (PDF: 25-829). No obvious shift of reflections as a consequence of the Dy^{3+} incorporation into the $NaGd(WO_4)_2$ lattice was detected, probably due to the similarity between the ionic radii of both lanthanide cations (1.027 Å for Dy^{3+} and 1.053 Å for Gd^{3+}, both octacoordinated). Nevertheless, the successful coprecipitation of the Gd^{3+} and Dy^{3+} cations was confirmed by ICP analysis, which indicated a Gd/(Dy + Gd) molar ratio of 0.56, which is close to the nominal value (0.5). The absorbance FTIR spectrum (Fig. 2b) of the synthesized NPs showed two bands at 3400 and 1625 cm^{-1}, attributed to adsorbed water, together with lattice vibration bands at <1000 cm^{-1}, characteristic of the tetragonal $NaLn(WO_4)_2$ phase.[36] Additionally, some absorptions were detected in the range of 1400 to 1550 cm^{-1}, which are due to the symmetric and asymmetric stretching vibrational modes of the PAA carboxylate anions.[37] This suggests that PAA molecules were adsorbed onto the surface of the NPs during the synthesis process. The amount of such molecules was determined from TG analysis (Fig. 2c), which showed an initial weight loss of 2.8% below 300 °C attributed to water desorption, followed by a second weight loss of 3.4% from 300 to 600 °C related to PAA decomposition. From now on, this sample will be labelled as $NaDy_{0.44}Gd_{0.56}(WO_4)_2$@PAA.

Dispersibility and colloidal stability in physiological media

To investigate the colloidal stability of our $NaDy_{0.44}Gd_{0.56}(WO_4)_2$@PAA NPs under physiological conditions, they were dispersed in water as well as in various simulated physiological media like MES and saline solution, and such dispersions were kept undisturbed at physiological temperature (37 °C) for different periods of time. We found that the hydrodynamic diameter (HD) values obtained by DLS for all as-prepared suspensions ($t = 0$) were only slightly higher (around 60 nm) than the NP size (Fig. 1b), and that such values did not change in a significant manner with an aging

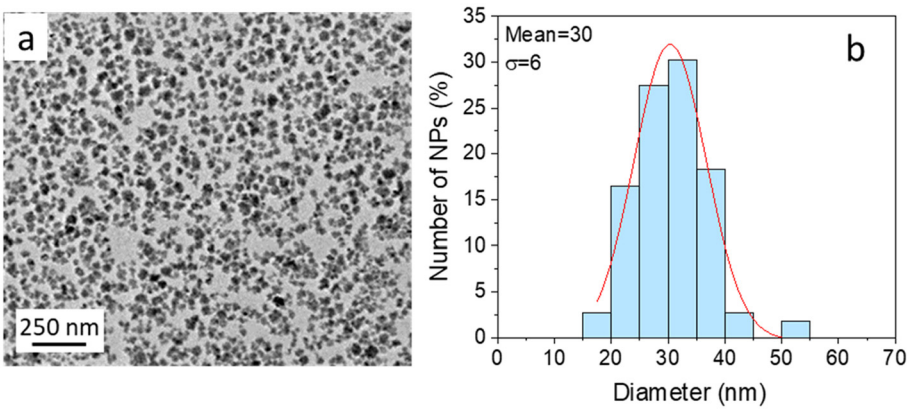

Fig. 1 TEM micrograph (a) and particle size histogram (b) of the synthesized NPs.

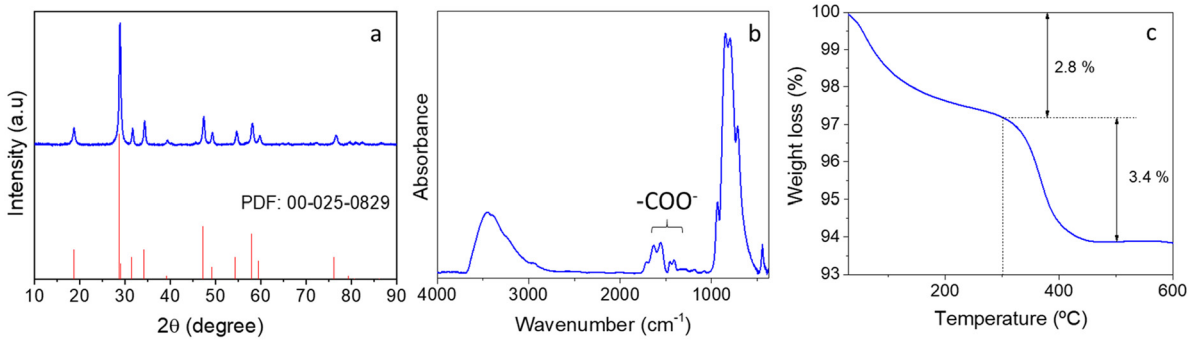

Fig. 2 XRD pattern (a), FTIR spectra (b), and thermogravimetry curve (c) of the synthesized NPs. The bottom ticks in (a) correspond to tetragonal $NaDy(WO_4)_2$ (25-829 PDF file). COO^- in (b) indicates the bands attributed to carboxylate ions.

time of at least up to 72 h (Fig. 3). This finding indicates high colloidal stability of our NPs under physiological conditions, as required for their use *in vivo*. Such behaviour is probably due to the presence of PAA molecules on the NP surface, preventing their aggregation through electrostatic and/or steric interactions.

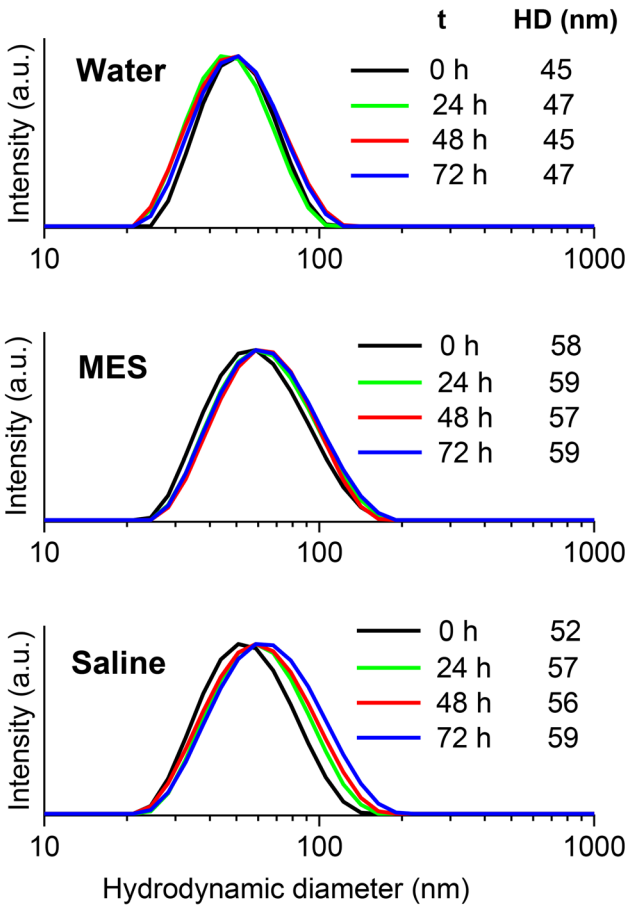

Fig. 3 DLS curves obtained for the $NaDy_{0.44}Gd_{0.56}(WO_4)_2$@PAA NPs dispersed in water, MES, and saline solution and aged undisturbed at 37 °C for different periods of time.

Cytotoxicity

The potential cytotoxicity of the $NaDy_{0.44}Gd_{0.56}(WO_4)_2$@PAA NPs was assessed using HFF-1 human foreskin fibroblasts as a model system, through a live–dead test, which shows cell morphology changes and necrotic and apoptotic processes, and the well-known MTT assay, which measures cell mitochondrial activity. For these analyses, the cells were incubated in the absence and the presence of different amounts of NPs dispersed in water with lanthanide (Gd + Dy) concentrations up to 100 μg mL^{-1}.

Fig. 4 shows the brightfield microscopy images obtained for cells incubated in the absence (Fig. 4a) and in the presence (Fig. 4b) of NPs with the highest assayed concentration corresponding to a total Ln^{3+} content of 100 μg mL^{-1}. No significant alterations of the cell morphology were detected, suggesting the biocompatibility of the NPs.

Regarding the live–dead test, Fig. 5a and b show the merging of brightfield microscopy images with fluorescence images obtained by staining the cells with Hoechst 33342 and TO-PRO-3, so that live cells appear in blue and dead cells in red. As observed, most cells show a blue colour. Consequently, there were no statistically significant differences ($p < 0.05$) detected in the percentage of deceased cells when subjected to Ln^{3+} concentrations up to 100 μg mL^{-1} compared to the negative control (Fig. 5c), suggesting the absence of late apoptosis. Finally, the analysis of the total cell counts per well for any of the tested Ln^{3+} concentrations (≤100 μg mL^{-1}) shows no significant decrease, with a p-value of <0.05 (Fig. 5d). This behaviour suggests that no cell necrosis took place after incubation with the studied NPs.

Finally, the MTT assay indicated that cell survival was clearly above 80% for NP concentrations up to 100 μg mL^{-1} (total Ln^{3+} content) (Fig. 6), indicating negligible cytotoxicity effects under the assayed conditions.

In vivo toxicity

The N2 *C. elegans* strain (wild-type) was incubated in the presence of $NaDy_{0.44}Gd_{0.56}(WO_4)_2$@PAA NPs to evaluate their *in vivo* biocompatibility. *C. elegans* employs rhythmic pharyngeal contractions to transport liquids into the intestinal lumen during feeding, so the worm ingests anything suspended in the medium. To visually assess the nematode's capacity for

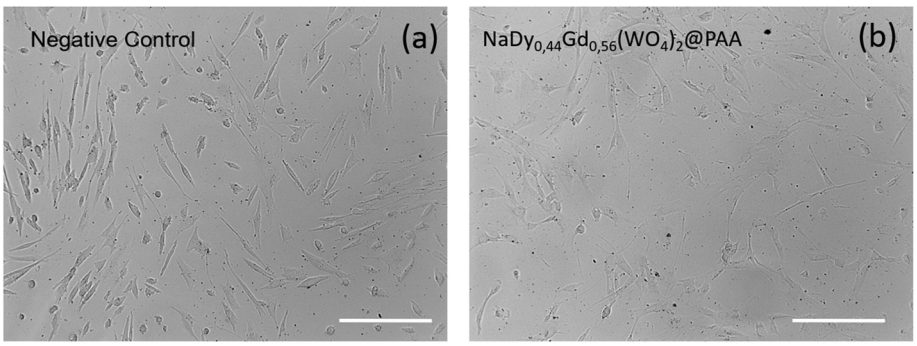

Fig. 4 Representative bright-field optical microscopy images of cells exposed to the $NaDy_{0.44}Gd_{0.56}(WO_4)_2$@PAA NPs at a concentration of 100 μg mL^{-1} of (Dy + Gd) (b) and negative control (a). The scale bar is 100 μm.

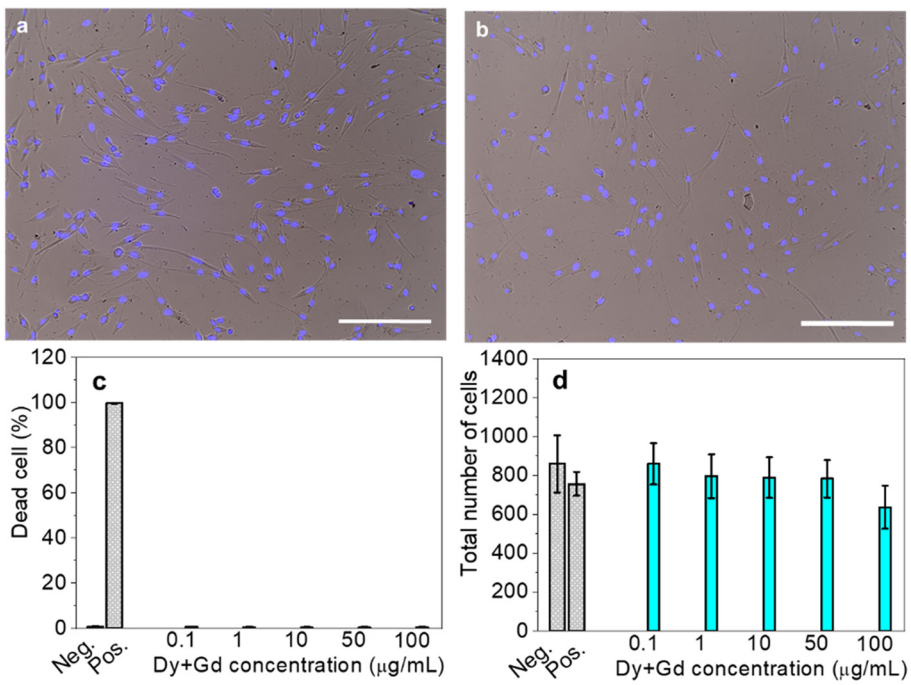

Fig. 5 Optical microscopy images of HFF-1 fibroblasts resulting from the merge of brightfield (grey), Hoechst 33342 (blue), and TO-PRO-3 iodine (red) images: negative control (a) and cells exposed to the $NaDy_{0.44}Gd_{0.56}(WO_4)_2$@PAA NPs at a concentration of 100 μg mL^{-1} of (Dy + Gd) (b). The scale bar is 100 mm. Percentage of dead cells (c) and total number of cells per well obtained from live–dead analysis (d). Error bars represent standard deviation.

consuming NPs, the worms that were exposed to a concentration of 1000 μg mL^{-1} of NPs were observed by TEM. The obtained images revealed the presence of NPs inside the nematode's intestine after treatment (Fig. 7), as supported by EDX analyses, confirming that the nematode ingested them.

A test of the end-point lethality of $NaDy_{0.44}Gd_{0.56}(WO_4)_2$@PAA was carried out at concentrations between 20 and 1000 μg mL^{-1}, without noting any toxic effects, even at the highest concentration of 1000 μg mL^{-1}, as shown in Fig. 8 (left). We also conducted a sub-lethal toxicity test (fertility), finding no harmful effects as indicated in Fig. 8 (right). Therefore, experiments conducted in *C. elegans* demonstrated the excellent *in vivo* biocompatibility of the $NaDy_{0.44}Gd_{0.56}(WO_4)_2$@PAA NPs.

Relaxivity properties

It is well known that magnetic relaxivity values are affected by the magnetic field strength.[38,39] In this work, we evaluated the r_1 and r_2 values of our $NaDy_{0.44}Gd_{0.56}(WO_4)_2$@PAA NPs at 1.44 and 3 T, which are the working conditions for most scanners commonly used in clinical practice.[40] As observed in Fig. 9, when increasing the applied magnetic field from 1.44 to 3 T, r_1 values decreased from 4.39 mM^{-1} s^{-1} to 3.43 mM^{-1} s^{-1} (Fig. 9a), while r_2 values increased from 6.76 to 12.56 mM^{-1} s^{-1} (Fig. 9b). The r_1 decrease agrees with the behavior predicted using the Solomon–Bloembergen–Morgan equations, which indicate that as a result of the increase of the electron

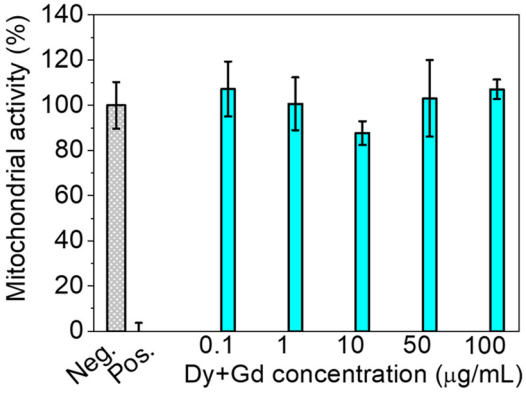

Fig. 6 Mitochondrial activity of cells exposed to increasing concentration (from 0.1 μg mL^{-1} to 100 μg mL^{-1} Dy + Gd) of the $NaDy_{0.44}Gd_{0.56}(WO_4)_2$@PAA NPs evaluated by MTT assay. Error bars represent standard deviation.

longitudinal spin relaxation time (T_{1e}) with increasing applied magnetic field, r_1 decreases.[41,42] On the other hand, the r_2 increase is explained by quantum-mechanical theory, according to which r_2 increases with increasing NP magnetization and therefore with increasing magnetic field.[39]

Importantly, the relaxivity values measured at both magnetic fields gave an r_2/r_1 ratio (1.54 at 1.44 T, and 3.6 at 3 T) within the range required for dual T_1–T_2 CAs (from 1 to 10).[4] In agreement, the T_1-weighted phantom images obtained at 3 T for aqueous dispersions of our NPs became brighter with increasing NP concentration, whereas the T_2-weighted ones became darker (Fig. 10). The relaxivities of our sample can be compared with those of Gd-DOTA, a commonly used commercial CA, which have been previously reported at different magnetic field strengths, including 3 T. For example, So *et al.* reported values of 7.07 mM^{-1} s^{-1} and 8.71 mM^{-1} s^{-1}, for r_1 and r_2, respectively.[43] Therefore, our NPs exhibited, as

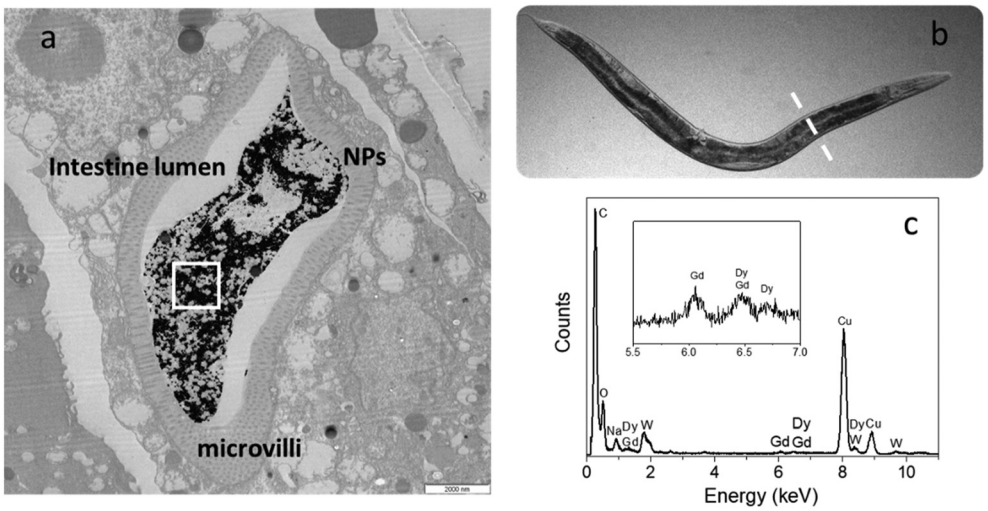

Fig. 7 Detailed TEM image (a) of the worm section (b) showing the intestine after NP exposition, and EDX spectrum (c) taken from the region marked with a white square in (a).

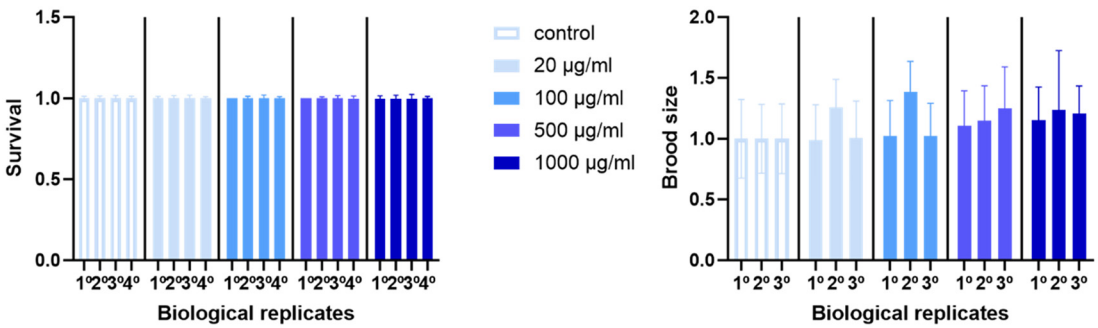

Fig. 8 Viability (left) and brood size (right) of N2 worms incubated at 20 °C with different $NaDy_{0.44}Gd_{0.56}(WO_4)_2$@PAA nanoparticle concentrations (μg mL^{-1}) for 24 h. Data were normalised to the mean of the control (worms not exposed to NPs). The mean + standard deviation is presented. Values for n = 4 independent experiments are given with 48 replicates per experiment at viability and n = 3 and 20 replicates for brood size. Statistical analysis was performed using nested ANOVA following Dunnett's multiple comparison test. No significant differences were observed between the treatment and control groups. Error bars represent standard deviation.

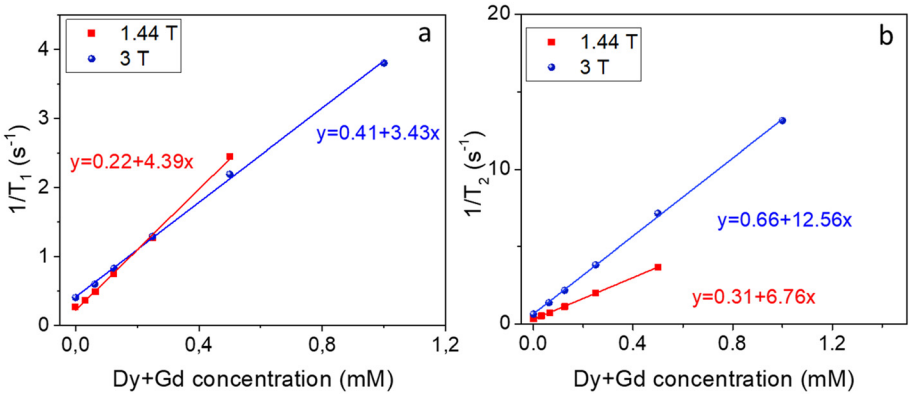

Fig. 9 Relaxation rates $1/T_1$ (a) and $1/T_2$ (b) measured at 1.44 and 3 T for aqueous dispersions of the $NaDy_{0.44}Gd_{0.56}(WO_4)_2$@PAA NPs at different concentrations.

expected, lower r_1 (3.43 mM^{-1} s^{-1}), but significantly higher r_2 (12.56 mM^{-1} s^{-1}) under comparable conditions. It must be finally noticed that the relaxivity values measured at 3 T for our $NaDy_{0.44}Gd_{0.56}(WO_4)_2$@PAA NPs were superior to the ones reported for mixed Gd/Dy fluoride-based NPs measured under the same magnetic field ($r_1 \leq 1.82$ mM^{-1} s^{-1} and $r_2 \leq 5.24$ mM^{-1} s^{-1}),[17] which manifests the superior performance of our NPs as a dual T_1–T_2 MRI CA.

X-Ray attenuation properties

The X-ray attenuation phantom images of aqueous suspensions of $NaDy_{0.44}Gd_{0.56}(WO_4)_2$@PAA NPs, along with those of iohexol solutions (a commercial iodine-based CT), are displayed in Fig. 11a. As observed, the contrast produced by our NPs is significantly higher than that of iohexol at any concentration, indicating the superior performance of our NPs as a CT CA. This behaviour can be quantified by plotting the X-ray

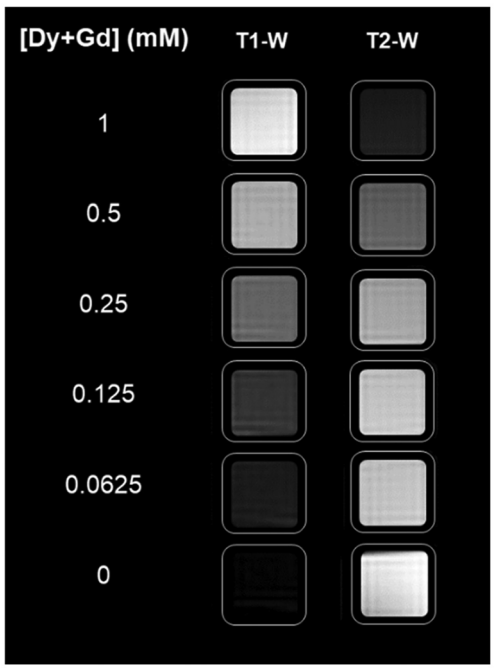

Fig. 10 Concentration-dependent T_1- and T_2-weighted phantom images of the $NaDy_{0.44}Gd_{0.56}(WO_4)_2$@PAA NPs at 3 T.

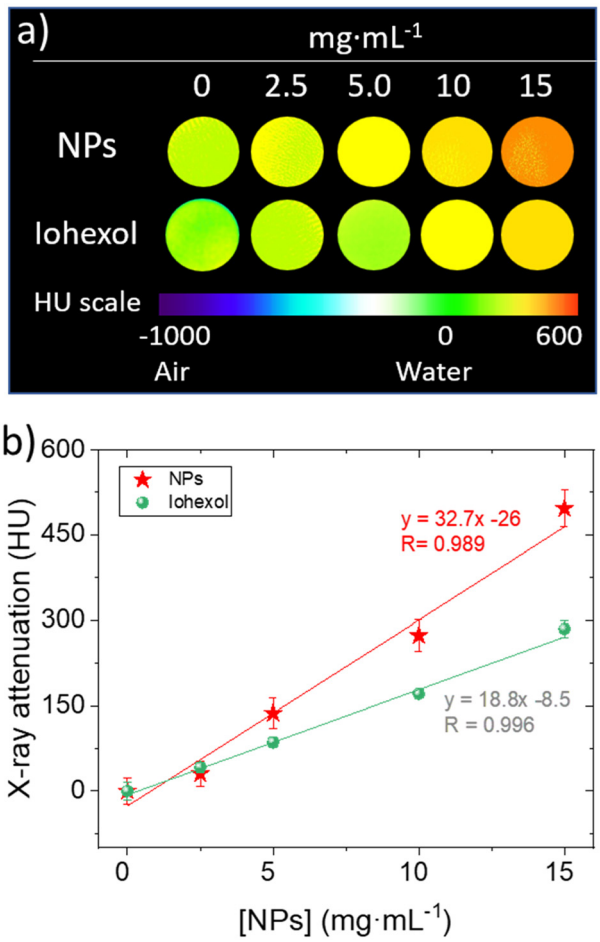

Fig. 11 X-ray attenuation phantom images (a) and values (in Hounsfield units, HU) (b) of $NaDy_{0.44}Gd_{0.56}(WO_4)_2$@PAA NPs and iohexol dispersed in water at different concentrations.

attenuation values in Hounsfield units (HU) *vs.* CA concentration (Fig. 11b). Such a plot results in straight lines, the slope of which, corresponding to the here-developed CA (32.7), is almost two times higher than that obtained for iohexol (18.8). This indicates that a much smaller amount of our NPs is needed to obtain a similar contrast, which is due to the higher atomic numbers of Dy (Z = 66), Gd (Z = 64), and mainly W (Z = 74) compared to that of I (Z = 53), as the X-ray attenuation coefficient increases with the fourth power of Z.[44] It should also be mentioned that the performance of our NPs was also higher than that reported for other Dy-based MRI contrast agents such as $DyVO_4$ (slope = 21.5),[45] which can also be explained by the higher Z value of W when compared with V (23).

Conclusions

We have addressed, for the first time in the literature, the suitability of sodium lanthanide tungstate ($NaDy_{0.44}Gd_{0.56}(WO_4)_2$)-based nanoparticles as dual T_1–T_2 MRI and CT contrast agents, aiming to improve the chemical stability drawback of previously reported lanthanide fluoride-based nanoparticles and, mainly, to increase their X-ray attenuation capability owing to the presence of tungsten. Such nanoparticles were successfully synthesized and coated with polyacrylic acid molecules by a wet chemistry method. They presented an almost spherical shape with a mean size of 30 nm and they were colloidally stable under conditions that mimic the physiological media, being noncytotoxic to the HFF-1 cell line. In addition, they did not show significant *in vivo* toxicity or repro-toxicity for *C. elegans* chosen as an animal model. The relaxivity values, measured under different magnetic fields used in clinical practice (1.44 and 3 T) for such nanoparticles, suggested that they were suitable as dual T_1–T_2 MRI CAs. Such relaxivity values were superior to the ones reported for mixed Gd/Dy fluoride-based NPs measured under the same magnetic field, which manifests the superior performance of our NPs as a dual T_1–T_2 MRI CA. Moreover, the nanoparticles displayed an X-ray attenuation capability higher than that of iohexol, a contrast agent frequently employed in clinics. All these characteristics make the here-developed sodium lanthanide (Dy^{3+}, Gd^{3+}) tungstate-based nanoparticles ideal bimodal probes for MRI and CT techniques.

Author contributions

M. Ocaña: conceptualization, supervision, formal analysis, funding acquisition and writing – original draft; E. Gómez-González: methodology, data curation, formal analysis, and writing – original draft; N. O. Nuñez: investigation, supervision, and writing – review & editing; C. Caro: data curation, formal analysis, and writing – review & editing; M. L. Garcia-Martín: funding acquisition, formal analysis, and writing – review & editing; J. M. Monje-Moreno: data curation, formal analysis, and writing – review & editing; A. Hamdi: data curation and formal analysis; P. López-Larrubia: funding acquisition, data curation, and formal analysis; A. I. Becerro: funding acquisition, data curation, and writing – review & editing.

Conflicts of interest

There are no conflicts to declare.

Data availability

The data that support the findings of this study are openly available in DIGITAL CSIC at https://doi.org/10.20350/digitalCSIC/17630.

Acknowledgements

This publication is part of the I + D + I Grants PID2021-122328OB-I00, PID2020-118448RB-C21 and PID2021-122528OB-I00, funded by MICIU/AEI/10.13039/501100011033 and by "ERDF A way of making Europe". Financial support was also provided by the Junta de Andalucía (P20_00182). DIAMOND network RED2022-134299-T funded by MICIN and grant PRE2019-090170 funded by MCIN/AEI/10.13039/501100011033 and by "ESF Investing in your future" are also acknowledged. Relaxivity measurements were performed at the ICTS "NANBIOSIS", specifically in Unit 28 at the "Instituto de Investigación Biomédica de Málaga y Plataforma en Nanomedicina (IBIMA Plataforma BIONAND)".

References

1 J. Key and J. F. Leary, Nanoparticles for multimodal in vivo imaging in nanomedicine, *Int. J. Nanomed.*, 2014, **9**, 711–726.
2 S. Caspani, R. Magalhaes, J. P. Araujo and C. T. Sousa, Magnetic nanomaterials as contrast agents for MRI, *Materials*, 2020, **13**, 2586.
3 M. J. Molaei, Gadolinium-doped fluorescent carbon quantum dots as MRI contrast agents and fluorescent probes, *Sci. Rep.*, 2022, **12**, 17681.
4 T. Tegafaw, S. Liu, M. Y. Ahmad, A. Saidi, D. Zhao, Y. Liu, S. W. Nam, Y. Chang and G. H. Lee, Magnetic Nanoparticle-Based High-Performance Positive and Negative Magnetic Resonance Imaging Contrast Agents, *Pharmaceutics*, 2023, **15**, 1745.
5 F. Q. Hu and Y. S. Zhao, Inorganic nanoparticle-based T_1 and T_1/T_2 magnetic resonance contrast probes, *Nanoscale*, 2012, **4**, 6235–6243.
6 M. Liu, J. Yuan, G. Wang, N. Ni, Q. Lv, S. Liu, Y. Gong, X. Zhao, X. Wang and X. Sun, Shape programmable T_1–T_2 dual-mode MRI nanoprobes for cancer theranostics, *Nanoscale*, 2023, **15**, 4694–4724.

7 P. Gowtham, K. Girigoswami, A. D. Prabhu, P. Pallavi, A. Thirumalai, K. Harini and A. Girigoswami, Hydrogels of Alginate Derivative-Encased Nanodots Featuring Carbon-Coated Manganese Ferrite Cores with Gold Shells to Offer Antiangiogenesis with Multimodal Imaging-Based Theranostics, *Adv. Ther.*, 2024, **7**, 2400054.

8 Y. Zhao, Y. Liu, Y. Wang, B. Xu, S. Zhang, J. Liu, T. Zhang, L. Jin, S. Song and H. Zhang, Rapidly clearable $MnCo_2O_4$@PAA as novel nanotheranostic agents for T_1/T_2 bimodal MRI imaging-guided photothermal therapy, *Nanoscale*, 2021, **13**, 16251–16257.

9 G. N. Wang, X. J. Zhang, A. Skallberg, Y. X. Liu, Z. J. Hu, X. F. Mei and K. Uvdal, One-step synthesis of water-dispersible ultra-small Fe_3O_4 nanoparticles as contrast agents for T_1 and T_2 magnetic resonance imaging, *Nanoscale*, 2014, **6**, 2953–2963.

10 M. P. Leal, S. Rivera-Fernandez, J. M. Franco, D. Pozo, J. M. de la Fuente and M. L. Garcia-Martin, Long-circulating PEGylated manganese ferrite nanoparticles for MRI-based molecular imaging, *Nanoscale*, 2015, **7**, 2050–2059.

11 G. K. Das, N. J. J. Johnson, J. Cramen, B. Blasiak, P. Latta, B. Tomanek and F. van Veggel, $NaDyF_4$ Nanoparticles as T_2 Contrast Agents for Ultrahigh Field Magnetic Resonance Imaging, *J. Phys. Chem. Lett.*, 2012, **3**, 524–529.

12 J. Wahsner, E. M. Gale, A. Rodriguez-Rodriguez and P. Caravan, Chemistry of MRI contrast agents: current challenges and new frontiers, *Chem. Rev.*, 2019, **119**, 957–1057.

13 S. Viswanathan, Z. Kovacs, K. N. Green, S. J. Ratnakar and A. D. Sherry, Alternatives to gadolinium-based metal chelates for magnetic resonance imaging, *Chem. Rev.*, 2010, **110**, 2960–3018.

14 S. Liu, H. Yue, S. Ho, S. Kim, J. Park, T. Tegafaw, M. Ahmad, S. Kim, A. Al Saidi, D. Zhao, Y. Liu, S. Nam, K. Chae, Y. Chang and G. Lee, Polyethylenimine-Coated Ultrasmall Holmium Oxide Nanoparticles: Synthesis, Characterization, Cytotoxicities, and Water Proton Spin Relaxivities, *Nanomaterials*, 2022, **12**, 1588.

15 J. Zhou, Z. G. Lu, G. G. Shan, S. H. Wang and Y. Liao, Gadolinium complex and phosphorescent probe-modified $NaDyF_4$ nanorods for T1- and T2-weighted MRI/CT/phosphorescence multimodality imaging, *Biomaterials*, 2014, **35**, 368–377.

16 Y. Zhang, G. K. Das, V. Vijayaragavan, Q. C. Xu, P. Padmanabhan, K. K. Bhakoo, S. T. Selvan and T. T. Y. Tan, "Smart" theranostic lanthanide nanoprobes with simultaneous up-conversion fluorescence and tunable T_1–T_2 magnetic resonance imaging contrast and near-infrared activated photodynamic therapy, *Nanoscale*, 2014, **6**, 12609–12617.

17 J. Y. Huang, Y. Hou, C. Y. Liu, L. H. Jing, T. C. Ma, X. D. Sun and M. Y. Gao, Chemical spacer design for engineering the relaxometric properties of core–shell structured rare earth nanoparticles, *Chem. Mater.*, 2015, **27**, 7918–7925.

18 X. Jin, F. Fang, J. Liu, C. Jiang, X. Han, Z. Song, J. Chen, G. Sun, H. Lei and L. Lu, An ultrasmall and metabolizable PEGylated $NaGdF_4$:Dy nanoprobe for high-performance T_1/T_2-weighted MR and CT multimodal imaging, *Nanoscale*, 2015, **7**, 15680–15688.

19 Z. Yi, X. Li, W. Lu, H. Liu, S. Zeng and J. Hao, Hybrid lanthanide nanoparticles as a new class of binary contrast agents for in vivo T_1/T_2 dual-weighted MRI and synergistic tumor diagnosis, *J. Mater. Chem. B*, 2016, **4**, 2715–2722.

20 D. Gonzalez-Mancebo, A. I. Becerro, T. C. Rojas, M. L. Garcia-Martin, J. M. de la Fuente and M. Ocana, HoF_3 and DyF_3 Nanoparticles as Contrast Agents for High–Field Magnetic Resonance Imaging, *Part. Part. Syst. Charact.*, 2017, **34**, 1700116.

21 D. Lisjak, O. Plohl, J. Vidmar, B. Majaron and M. Ponikvar-Svet, Dissolution Mechanism of Upconverting AYF_4:Yb,Tm (A = Na or K) Nanoparticles in Aqueous Media, *Langmuir*, 2016, **32**, 8222–8229.

22 M. I. Saleh, B. Ruhle, S. Wang, J. Radnik, Y. You and U. Resch-Genger, Assessing the protective effects of different surface coatings on $NaYF_4$:Yb^{3+}, Er^{3+} upconverting nanoparticles in buffer and DMEM, *Sci. Rep.*, 2020, **10**, 19318.

23 S. Guth, S. Hueser, A. Roth, G. Degen, P. Diel, K. Edlund, G. Eisenbrand, K.-H. Engel, B. Epe, T. Grune, V. Heinz, T. Henle, H.-U. Humpf, H. Jaeger, H.-G. Joost, S. E. Kulling, A. Lampen, A. Mally, R. Marchan, D. Marko, E. Muehle, M. A. Nitsche, E. Roehrdanz, R. Stadler, C. van Thriel, S. Vieths, R. F. Vogel, E. Wascher, C. Watzl, U. Noethlings and J. G. Hengstler, Toxicity of fluoride: critical evaluation of evidence for human developmental neurotoxicity in epidemiological studies, animal experiments and in vitro analyses, *Arch. Toxicol.*, 2020, **94**, 1375–1415.

24 T. Tegafaw, W. Xu, M. W. Ahmad, J. S. Baeck, Y. Chang, J. E. Bae, K. S. Chae, T. J. Kim and G. H. Lee, Dual-mode T_1 and T_2 magnetic resonance imaging contrast agent based on ultrasmall mixed gadolinium-dysprosium oxide nanoparticles: synthesis, characterization, and in vivo application, *Nanotechnology*, 2015, **26**, 365102.

25 E. Gómez-González, N. O. Núñez, C. Caro, M. L. García-Martín, A. I. Becerro and M. Ocaña, Lanthanide vanadate-based nanoparticles as multimodal T_1-T_2 MRI contrast agent and NIR luminescent imaging probe, *J. Alloys Compd.*, 2024, **1003**, 175647.

26 A. N. Generalova, B. N. Chichkov and E. V. Khaydukov, Multicomponent nanocrystals with anti-Stokes luminescence as contrast agents for modern imaging techniques, *Adv. Colloid Interface Sci.*, 2017, **245**, 1–19.

27 L. Prodi, E. Rampazzo, F. Rastrelli, A. Speghini and N. Zaccheroni, Imaging agents based on lanthanide doped nanoparticles, *Chem. Soc. Rev.*, 2015, **44**, 4922–4952.

28 C. Caro, M. Dalmases, A. Figuerola, M. L. Garcia-Martin and M. Pernia Leal, Highly water-stable rare ternary Ag–Au–Se nanocomposites as long blood circulation time X-ray computed tomography contrast agents, *Nanoscale*, 2017, **9**, 7242–7251.

29 E. Gomez-Gonzalez, N. O. Nunez, C. Caro, M. Garcia-Martin, Y. Fernandez-Afonso, J. M. de la Fuente,

M. Balcerzyk and M. Ocana, Dysprosium and holmium vanadate nanoprobes as high-performance contrast agents for high-field magnetic resonance and computed tomography imaging, *Inorg. Chem.*, 2021, **60**, 152–160.

30 R. Calderón-Olvera, N. O. Núñez, D. González-Mancebo, J. Monje-Moreno, M. Muñoz-Rui, E. Gómez-González, E. Arroyo, B. Torres-Herrero, J. de la Fuente and M. Ocaña, Europium doped-double sodium bismuth molybdate nanoparticles as contrast agents for luminescence bioimaging and X-ray computed tomography, *Inorg. Chem. Front.*, 2023, **10**, 3202–3212.

31 L. Gonzalez-Moragas, A. Roig and A. Laromaine, C. elegans as a tool for in vivo nanoparticle assessment, *Adv. Colloid Interface Sci.*, 2015, **219**, 10–26.

32 L. Alvino, M. Pacheco-Herrero, A. Lopez-Lorente, Z. Quiñones, S. Cárdenas and Z. González-Sánchez, Toxicity evaluation of barium ferrite nanoparticles in bacteria, yeast and nematode, *Chemosphere*, 2020, **254**, 126786.

33 L. Girard, T. Fiedler, T. Harris, F. Carvalho, I. Antoshechkin, M. Han, P. Sternberg, L. Stein and M. Chalfie, WormBook: the online review of Caenorhabditis elegans biology, *Nucleic Acids Res.*, 2007, **35**, D472–D475.

34 E. Gómez-González, C. Caro, N. O. Núñez, D. González-Mancebo, J. Urbano-Gámez, M. L. Garcia-Martin and M. Ocaña, Sodium lanthanide tungstate-based nanoparticles as bimodal contrast agents for in vivo high-field MRI and CT imaging, *J. Mater. Chem. B*, 2024, **12**, 11123–11133.

35 E. Gomez-Gonzalez, C. Caro, D. Martinez-Gutierrez, M. L. Garcia-Martin, M. Ocana and A. Becerro, Holmium phosphate nanoparticles as negative contrast agents for high-field magnetic resonance imaging: Synthesis, magnetic relaxivity study and in vivo evaluation, *J. Colloid Interface Sci.*, 2021, **587**, 131–140.

36 M. Li, J. Wu, H. Jia, M. Wang and Z. Liu, Luminescence properties and energy transfers of $NaLa(WO_4)_2$:Sm^{3+}:Ce^{3+} phosphor, *J. Mater. Sci.:Mater. Electron.*, 2019, **30**, 10465–10474.

37 L. J. Kirwan, P. D. Fawell and W. van Bronswijk, In situ FTIR-ATR examination of poly (acrylic acid) adsorbed onto hematite at low pH, *Langmuir*, 2003, **19**, 5802–5807.

38 P. Caravan, C. T. Farrar, L. Frullano and R. Uppal, Influence of molecular parameters and increasing magnetic field strength on relaxivity of gadolinium– and manganese–based T_1 contrast agents, *Contrast Media Mol. Imaging*, 2009, **4**, 89–100.

39 M. Norek, E. Kampert, U. Zeitler and J. A. Peters, Tuning of the Size of Dy_2O_3 Nanoparticles for Optimal Performance as an MRI Contrast Agent, *J. Am. Chem. Soc.*, 2008, **130**, 5335–5340.

40 E. Gomez-Gonzalez, C. Caro, M. L. Garcia-Martin, A. I. Becerro and M. Ocaña, Outstanding MRI contrast with dysprosium phosphate nanoparticles of tuneable size, *Nanoscale*, 2022, **14**, 11461–11470.

41 M. Rohrer, H. Bauer, J. Mintorovitch, M. Requardt and H. J. Weinmann, Comparison of magnetic properties of MRI contrast media solutions at different magnetic field strengths, *Invest. Radiol.*, 2005, **40**, 715–724.

42 I. M. Noebauer-Huhmann, P. Szomolanyi, V. Juras, O. K. Dipl, M. E. Ladd and S. Trattnig, Gadolinium-based magnetic resonance contrast agents at 7 Tesla: in vitro T: 1: relaxivities in human blood plasma, *Invest. Radiol.*, 2010, **45**, 554–558.

43 Y. H. So, W. Lee, E. A. Park and P. K. Kim, Investigation of the Characteristics of New, Uniform, Extremely Small Iron-Based Nanoparticles as T_1 Contrast Agents for MRI, *Korean J. Radiol.*, 2021, **22**, 1708–1718.

44 D. González-Mancebo, A. I. Becerro, A. Corral, M. Moros, M. Balcerzyk, J. M. de la Fuente and M. Ocana, Enhancing Luminescence and X-ray Absorption Capacity of Eu^{3+}:LaF_3 Nanoparticles by Bi^{3+} Codoping, *ACS Omega*, 2019, **4**, 765–774.

45 E. Gomez-Gonzalez, D. Gonzalez-Mancebo, N. O. Nunez, C. Caro, M. L. Garcia-Martin, A. I. Becerro and M. Ocana, Lanthanide vanadate-based trimodal probes for near-infrared luminescent bioimaging, high-field magnetic resonance imaging, and X-ray computed tomography, *J. Colloid Interface Sci.*, 2023, **646**, 721–731.